Arash Abbasnia
Mahmoud Ghiasi

ISSN 1333-1124
eISSN 1849-1391

NUMERICAL PREDICTION OF HYDROFOIL PERFORMANCE IN WAVE BY NURBS NUMERICAL WAVE TANK

Summary

Time domain simulation using a Mixed Eulerian-Lagrangian (MEL) formulation and a high-order boundary integral method based on the Non-Uniform Rational B-spline (NURBS) formulation is employed to develop a Numerical Wave Tank (NWT). At each time step the Laplace equation is solved in the Eulerian frame and fully nonlinear free surface conditions are updated in the Lagrangian manner through a time marching scheme. Two damping zones are adopted at both ends of the tank to reduce the reflected wave energy. The fully nonlinear free surface simulations by different orders of B-spline basis functions in the NWT are examined through the volume, momentum and energy conservation. Hydrofoil performance in wave is considered for the practical application of the fully nonlinear NWT. Thrust and lift coefficients of a foil are computed and compared with the experimental data and other numerical solutions. Instantaneous forces and pressure distribution over the foil body are also computed.

Key words: *Numerical wave tank, Mixed Eulerian-Lagrangian method, B-spline, Potential flow, Hydrofoil*

1. Introduction

A numerical wave tank (NWT) has been developed to investigate a fully nonlinear simulation of various phenomena in ocean engineering including wave propagation, wave deformation, and wave body interaction. In the past three decades, a great deal of effort has been made to develop computational tools equivalent to a physical wave tank. In general, these attempts are categorized into potential and viscous NWTs. Most of the work has been focused on obtaining fully nonlinear, inviscid time-domain solutions for wave generation and propagation problems in both two and three dimensions. The most popular approach taken in NWT is the Mixed Eulerian-Lagrangian (MEL) time-marching method developed by Longuet-Higgins and Cokelet [10]. The MEL scheme requires solving the Laplace equation at each time step in the Eulerian frame and updating the moving boundary points and values in the Lagrangian manner. The velocity potential at each time step is computed by a boundary integral equation method in the fluid control volume.

The disturbance of fluid particles arises from putting a wave maker on the upstream boundary. Wave makers are sorted into two classes. One is a physical wave generator that

looks like a wave maker in a physical wave tank and moves with prescribed motion. The other one is an artificial wave generator which is used on the inflow boundary to distribute sources in the fixed vertical space. Since the inflow boundary is not involved in the boundary updating, the wave characteristics could be specified as a disturbance source for the wave generator. A review on different types of wave makers is presented in detail by Tanizawa [14] and Newman [11].

To prevent wave reflection from the wall at the ends of the wave tank, wave absorbers are adopted at the upstream and downstream boundaries. This function is essential for maintaining the unbounded region condition during a lengthy simulation and for avoiding the non-physical manner of the propagating wave reflected from the end walls within the computational domain. Wave absorbing methods used in NWTs are grouped into three categories. The simplest one is an active wave absorber used as the absorbing beach of a real wave tank. The second approach is Sommerfeld's radiation condition that was adopted in linear free surface problems. The adoption of this scheme is a little tricky for nonlinear time domain simulations. The third one includes artificial wave absorbing methods named as sponge layer, artificial beach, and damping zone used as passive wave absorption.

The boundary element method is used to solve the Laplace equation in potential flow problems. Solving the Laplace equation in the Eulerian manner is classified into direct and indirect methods. Description of boundary geometry and distribution of potential velocity over the boundary may affect the precision of boundary integral implementation. The indirect method is applied in NWT by Zhang et al. [18] to model the linear and the nonlinear wave propagation and wave shoaling on a submerged obstacle.

The direct method has been widely used with different formulations. The constant element, as the simplest one, is employed by Ryu et al. [13] to simulate the current-wave interaction in the two-dimensional NWT. The linear elements formulation is an efficient approach used by Büchmann et al. [3] to predict the wave run-up on a structure. Analogously, this method was used to determine the Bragg condition.

Reflection in a potential NWT is discussed by Tang et al. [15]. Boundary description with curvilinear elements was presented by Baudic et al. [1] in a nonlinear two-dimensional potential wave tank so that a cubic shape function over each four-node element is applied to describe the variation in the geometry and in the boundary functions.

By substituting the normal flux and tangential derivation of free surface potential into the free surface boundary condition, the velocity and time derivation of the potential of free surface water particles can be obtained in each time step. Variables of the geometry and velocity potential function of free surface are updated in the Lagrangian manner for the next time step. The time integration method in a time domain simulation is efficient to keep stability and precision of the solution. The first order and the second order finite difference scheme were employed at each time step as a low-order time stepping method in NWTs by Wu & Tsay [16], Xiao et al. [17] and Ryu et al. [13] to find new boundary values and the geometry for the next time step. High-order approaches were used by Koo [8] (4th order Runge-Kutta method) and by Zhang et al. [18] (5th order Runge-Kutta-Gil and 4th order Adams-Bashforth-Moulton method).

In the wave propagation problem, a discontinuity of flux, called the corner problem, which occurs at the intersection of the free surface and the tank wall surface, affects the solution stability severely. To overcome this difficulty, some remedies have been proposed. The double-node technique, developed by Grilli et al. [6], is suitable for NWTs. The other approach is that of discontinuous elements recommended by Brebbia [2]. The two techniques are compared in the standing wave problem by Hamano et al. [7].

During the free surface simulation of nonlinear waves, the non-physical saw-tooth instability may occur. Instabilities may also arise from a variable mesh size or natural singular treatment at the intersection of the wave maker and the free surface. To remedy the saw-tooth instability, smoothing schemes have been used, such as the Chebyshev five-point smoothing scheme, Koo and Kim [9], and the B-spline smoothing scheme.

In the present paper, nonlinear wave propagation is analyzed by a 2D fully nonlinear numerical wave tank. The NWT is developed based on the potential theory, mixed Eulerian-Lagrangian approach, and high-order boundary element method. The material node approach scheme is treated as a time-marching scheme. The time-marching scheme consists of the following routines at each time step: (a) solving the Laplace equation in the Eulerian frame, (b) updating the moving collocation points on the boundary and specified values in the Lagrangian manner. The two damping zones proposed by Cointe [4] are implemented at the ends of the tank to absorb the wave reflection from the end wall and the wave maker. The wave maker is provided by specifying wave characteristics of one of the wave theories on the fixed inflow boundary.

This paper is mainly focused on the development of the boundary integral method based on the Non-Uniform Rational B-spline (NURBS) formulation coupled with the Mixed Eulerian Lagrangian (MEL) formulation to simulate propagation in a nonlinear numerical wave tank. The direct boundary element method is employed to solve the potential flow boundary value problem. Discretization of the computational domain boundary and distribution of potential velocity over the boundary are based on the NURBS as a high-order interpolation function. The Gaussian-quadrature numerical integration approach is adopted as a high-order non-uniform numerical integration scheme. The fourth order Runge-Kutta is used for the time stepping integration of free surface boundary conditions and geometry. The position of instantaneous free surface is traced by applying the material node approach while the re-gridding of the free surface has to be done at each time-step. The non-physical saw-tooth instability is solved via the Chebyshev five-point smoothing scheme. Computations of the second order Stokes wave propagation in the NURBS NWT are verified by analytical solutions. Different orders of B-spline basis functions in the fully nonlinear free surface approximation are examined through volume, momentum and energy conservation.

In addition, a hydrofoil is put into the numerical wave tank to examine the computational procedure. A zero flux foil body boundary condition is added to the integration surface. The vortex problem arising from potential discontinuity at the trailing edge is treated through the distribution of constant strength dipoles over the wake surface extended between the trailing edge and the tank end wall. The foil performance in wave is compared with experimental results and other computational solutions. Time history of forces and pressure distribution over the foil body are presented. Numerical results for a hydrofoil show that the present high-order model is successful in the simulation of nonlinear phenomena in the fully nonlinear numerical wave tank.

2. Theoretical development

In this article, the fluid is assumed to be homogeneous, incompressible, and inviscid and its motion is irrotational. Consider the boundary value problem with a potential $\phi(x,z,t)$, which satisfies Laplace's equation in a finite two-dimensional control domain R.

$$\nabla^2\phi = 0 \quad \text{in } R \tag{1}$$

A Cartesian coordinate system (x,z) is taken. The x-axis lies on the still water level and the z-axis is directed vertically upward (see Figure 1). The NWT has a constant depth d

and the damping zones are located at the both ends. Flow about a hydrofoil with an angle of attack θ, cord length c and submergence depth d_0 underneath of wavy free surface is computed in the time domain. To solve the boundary value problem, boundary conditions are required on the bottom, free surface, hydrofoil surface, input and output boundaries.

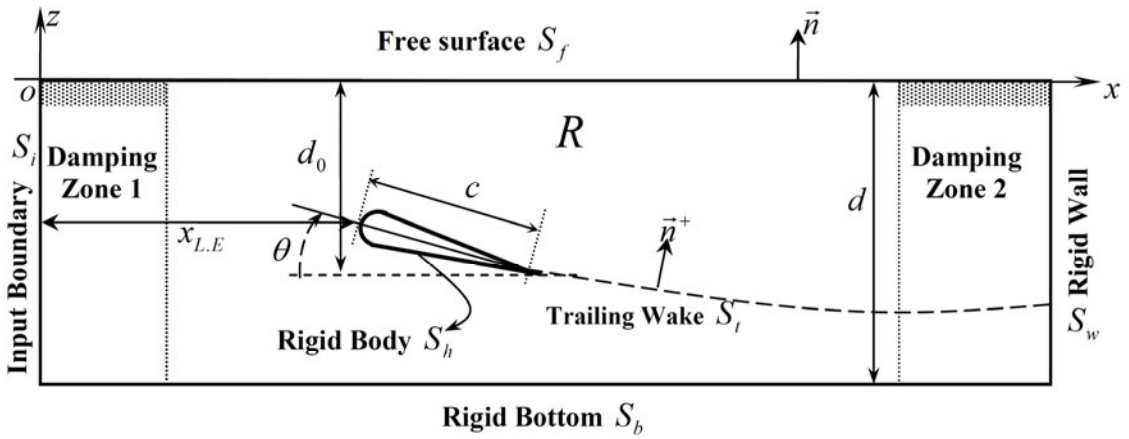

Fig. 1 Definition sketch

2.1 Boundary conditions and initial condition

There are two fully nonlinear boundary conditions on the free surface (S_f), the kinematic (KFSBC) and the dynamic boundary condition (DFSBC), as defined below.

$$\begin{aligned} &\frac{\partial \eta}{\partial t} = \frac{\partial \phi}{\partial z} - \frac{\partial \phi}{\partial x}\frac{\partial \eta}{\partial x} \quad \text{(KFSBC)} \\ &\frac{\partial \phi}{\partial t} = -gz - \frac{1}{2}\left|\nabla \phi\right|^2 \quad \text{(DFSBC)} \end{aligned} \quad \text{on } S_f \tag{2}$$

Both boundary conditions are satisfied on the exact free surface, in which $\eta(x,t)$ is the wave elevation measured from the still water level, ϕ is the free surface potential, t shows the time of simulation, and g is the gravitational acceleration. Impermeable condition is applied in the solution by the zero-flux potential on the rigid bottom boundary (S_b), the foil body (S_h) and the wall boundary at the wave tank end (S_w).

$$\frac{\partial \phi}{\partial n} = 0 \quad \text{on } S_b, S_h \text{ and } S_w \tag{3}$$

Normal vector ($\vec{n}$) in the control domain is directed outwards. Equation (3) states that the velocity of water particles in the normal direction ($\partial\phi/\partial n$) to the boundary vanishes. Normal velocity at the input boundary (S_i) is given based on the known incident velocity potential functions (ϕ_{wg}).

$$\frac{\partial \phi}{\partial n} = -\frac{\partial \phi_{wg}}{\partial x} \quad \text{on } S_i \tag{4}$$

According to Koo and Kim [9], the nonlinear second order Stokes wave theory is applied to the input boundary condition.

$$\frac{\partial \phi_{wg}}{\partial x} = \frac{gAk}{\omega} \frac{\cosh\left(k\left(z+d\right)\right)}{\cosh(kd)} \cos\left(kx-\omega t\right) + \frac{3}{4} A^2 \omega k \frac{\cosh\left(2k\left(z+d\right)\right)}{\sinh^4(kd)} \cos 2\left(kx-\omega t\right) \tag{5}$$

where A, k, ω, d, and t are the wave amplitude, wave number, angular frequency, water depth, and time, respectively. The wave number is obtained by dispersion relation.

$$\omega^2 = gk \tanh\left(kd\right) \tag{6}$$

The incident wave on the inflow boundary is increased gradually by using a ramping function which smoothly approaches unity from zero. The ramping function is used to reduce the transient effect so that the numerical solution becomes stable and reaches the steady state properly. In the present modelling, the following ramping function is used:

$$f_m\left(t\right) = \begin{cases} \frac{1}{2}\left(1-\cos\frac{\pi t}{T_m}\right), & t \le T_m \\ 1, & t > T_m \end{cases} \tag{7}$$

in which, T_m is the modulation time. Initial conditions for the initial free surface value are

$$\begin{aligned} &\eta\left(x, t \le 0\right) = 0 \\ &\phi\left(x, z, t \le 0\right) = 0 \end{aligned} \tag{8}$$

Boundary integral equation based on Green's second identity is employed to solve the boundary value problem:

$$c_i \phi_i = \int_{\Gamma} \left(G \frac{\partial \phi_j}{\partial n} - \phi_j \frac{\partial G}{\partial n} \right) \mathrm{d}\Gamma - \int_{S_t} \Delta\phi_t \frac{\partial G}{\partial n^+} \mathrm{d}S, \tag{9}$$

where $c_i = \theta'/2\pi$, θ' is the internal angle at a point i on the boundary of the computational domain ($\Gamma \in S_i \bigcup S_b \bigcup S_h \bigcup S_w \bigcup S_f$); and for two-dimensional problems,

$$G = \frac{1}{2\pi} \ln\left(\frac{1}{r}\right), \tag{10}$$

which represents the flow field generated by a concentrated unit source acting as the singular source. The second integral of Equation (9) is related to the distribution of singularity on the wake surface S_t. $\Delta\phi_t$ is the potential difference across the trailing wake and $\vec{n}^+$ is the normal vector on the wake surface directed upwards. The trailing edge of the foil and the intersection of the wake surface and the wave tank end, where two vortices are positioned, represent the trailing wake surface.

2.2 High-order boundary element

By discretization of the boundary integral equation, a linear system of equations can be obtained. The inflow boundary, end-wall boundary, and bottom boundary are described exactly by linear elements and the Gaussian eight-point quadrature integration is employed for calculating the boundary integral on each element. Since the free surface boundary as a

moving boundary is severely fluctuating and must be updated at each time step, linear elements are not able to model this oscillatory free surface precisely. Exact geometry description and parameters of a complicated boundary such as normal vector, length, area, and spatial derivative of boundary values are significant advantages of curvilinear elements. Piegl and Tiller [12] summarized parametric interpolation functions which approximate arbitrary curves and surfaces in computational modelling, such as Bezier, B-spline, and non-rational uniform B-spline curve (surface). The NURBS curve is described as:

$$C(u)=\left(x(u),z(u)\right)=\frac{\sum_{i=1}^{n}N_i^{(p)}(u)P_i\omega_i}{\sum_{i=1}^{n}N_i^{(p)}(u)\omega_i} \tag{11}$$

where x and z represent the positions of the points on the NURBS curve. The knot vector u is the parametric value of the NURBS curve and n is the number of control points in the u direction, $(0\le u\le 1)$. P_i and ω_i are the control points and the weighted function, respectively. $N_i^{(p)}(u)$ is the basis function with a degree of p in the u direction. When the free surface is represented by a set of data, it is convenient to model the free surface by the NURBS curve. Equation (11) provides a system of n linear equations for known curve data points, χ_k, and the unknown P_i. Using homogeneous coordinates, Equation (11) is decomposed into a set of linear equations.

$$\sum_{i=1}^{n}\Re_i^{(p)}(\bar{u}_m)P_i=\chi_m \quad , \; m=1,...,n \tag{12}$$

where

$$\Re_i^{(p)}(u)=\frac{N_i^{(p)}(u)\omega_i}{\sum_{j=0}^{n}N_j^{(p)}(u)\omega_j} \tag{13}$$

Using $\bar{u}_m$ as the value of knots, the position of control points, P_i, can be obtained by computing the n value of rational functions $\Re_1^{(p)},...,\Re_n^{(p)}$. $\bar{u}_m$ can be obtained as follows:

$$\bar{u}_m=\bar{u}_{m-1}+\frac{\left|\chi_m-\chi_{m-1}\right|}{l} \quad \text{for} \; m=2,...,n-1 \tag{14}$$

where $l=\sum_{m=1}^{n}\left|\chi_m-\chi_{m-1}\right|$.

To solve the boundary integral equation, the Gaussian points are selected on the free surface and the parameters of the Gaussian points are computed based on the NURBS. The Gaussian points Q on the free surface, which are used as the collocation points, can be described by

$$Q(u)=\left(x(u),z(u)\right) \tag{15}$$

The unit tangent vector ($\vec{s}$) for the collocation points Q_i in the u direction can be defined as

$$\vec{s}=s_x\vec{i}+s_z\vec{k}=\frac{\vec{T}_u}{\left|\vec{T}_u\right|}, \tag{16}$$

where $\vec{T}_u$ is the tangent vector along the u direction.

$$\vec{T}_u = \frac{\partial x}{\partial u}\vec{i} + \frac{\partial z}{\partial u}\vec{k} \tag{17}$$

The unit normal vector $\vec{n}$ at the point Q can be found from

$$\vec{n} = \frac{-\frac{\partial z}{\partial u}\vec{i} + \frac{\partial x}{\partial u}\vec{k}}{\left|\vec{T}_u\right|} \tag{18}$$

2.3 Time marching scheme

At each instant, the fully nonlinear free surface boundary condition is updated through the Runge-Kutta fourth order time integration scheme and the MEL approach to find the new boundary position and the value for the next time step. If the velocity of the free-surface node motion is represented by $\vec{\upsilon}$, the material derivative will be formulated in the $\left(\delta/\delta t = \partial/\partial t + \vec{\upsilon}\cdot\nabla\right)$ form. Then, the fully nonlinear free-surface boundary conditions in the Lagrangian frame are formed as:

$$\begin{aligned} \frac{\delta\phi}{\delta t} &= -g\eta - \frac{1}{2}\left|\nabla\phi\right|^2 + \nabla\phi\cdot\vec{\upsilon} \\ \frac{\delta\eta}{\delta t} &= \frac{\partial\phi}{\partial z} - \left(\nabla\phi - \vec{\upsilon}\right)\cdot\nabla\eta \end{aligned} \tag{19}$$

In the present study, the collocation points on the free surface are moving with the water particle motion $\left(\vec{\upsilon} = \nabla\phi\right)$, which is called a material node approach. Specifically, when the material node approach is adopted, Equation (19) will be modified as

$$\begin{aligned} \frac{\delta\phi}{\delta t} &= -g\eta + \frac{1}{2}\left|\nabla\phi\right|^2 \\ \frac{\delta\vec{\ell}}{\delta t} &= \nabla\phi \end{aligned} \tag{20}$$

where $\vec{\ell}$ is the location of free surface nodes $\left(x, z\right)$ with respect to the Cartesian coordinate system origin.

2.4 Numerical wave absorption

To obtain appropriate numerical solutions to the wave propagation problem in a numerical wave tank, artificial damping zones (sponge layers) are used at both ends of the wave tank to retain the unbounded condition so that the wave energy is absorbed progressively to reduce wave reflection from the ends of the wave tank. When simulating in a physical wave tank, however, the re-reflection takes place and no prevention is required. But in a NWT, a damping zone is prepared in front of the wave maker to dissipate the reflected wave before it reaches the wave maker. The energy dissipation scheme includes adding an artificial damping term to the fully nonlinear free surface boundary conditions over the specific regions of the free surface adjacent to the inflow boundary and the end wall boundary. Modified nonlinear free surface boundary conditions with the damping coefficient presented by Cointe [4] are as follows:

$$\begin{aligned} \frac{\delta\phi}{\delta t} &= -g\eta + \frac{1}{2}\left(\nabla\phi\cdot\nabla\phi\right) - \nu\left(x\right)\left(\phi-\phi_e\right) \\ \frac{\delta\vec{\ell}}{\delta t} &= \nabla\phi - \nu\left(x\right)\left(\vec{\ell}-\vec{\ell}_e\right) \end{aligned} \quad \text{on } S_f \tag{21}$$

where the subscript e corresponds to the reference configuration of the fluid. The function $\nu\left(x\right)$ is the damping coefficient given by

$$\nu\left(x\right) = \alpha\omega\left[\frac{k}{2\pi}\left(x-x_0\right)\right]^2 \quad , \; x_0 \le x \le x_1 = x_0 + \frac{2\pi\beta}{k} \tag{22}$$

In practice, the damping coefficient is equal to zero except in the damping zone $\left(x_0 \le x \le x_1\right)$, which is continuous and continuously differentiable, and is tuned to the characteristic wave frequency (ω) and the characteristic wave number (k). Strength and length of the damping zone are controlled by the dimensionless parameters α and β, respectively. The terms ϕ_e and $\vec{\ell}_e = \left(x_e, z_e\right)$ are the reference values. These damping terms absorb differences between the reference value and the simulated values. When the reference values are set to the calm water condition ($\phi_e = 0$, $z_e = 0$), the damping zone acts as a simple absorber. If a propagating wave is used as a reference value, the damping zone allows only this wave to pass through.

2.5 Smoothing scheme

The simulation of nonlinear wave motions requires attention to maintain numerical accuracy and avoid instability in a lengthy simulation. In the MEL method, a smoothing scheme is used in time marching to avoid the saw tooth instability which occurs during the free surface simulation of a highly nonlinear wave. In this paper, the variable node space Chebyshev five-point smoothing scheme is applied to remove these non-physical oscillations.

2.6 Corner problem in the tank boundary intersection

At the intersection of the free surface and the tank walls, as well as at the intersection of the bottom and the tank walls, singularity in the solution occurs due to the discontinuity of normal vector on the boundary (Figure 2). Stability of the solution in a NWT depends greatly on intersection singularities. To remove this discontinuity, different techniques have been developed. In this paper, the double node technique is adopted to handle the corner point problem. The free surface boundary as a moving boundary is updated in every time step. Approximation of intersection point velocity at the junction of the free surface elevation and the inflow and the outflow boundary would be required. As a matter of fact, at the inflow intersection points, the known values include the potential and the potential flux before the corner and the unknown value is the potential flux after the corner point. As shown in Figure 2, points P_w and P_f are the double nodes collocated at the same position, and $\vec{n}_f = \left(n_{fx}, n_{fz}\right)$ is the unit normal vector of the free surface while $\vec{n}_w = \left(n_{wx}, n_{wz}\right)$ is that of the wall surface. Since the intersection is a vertex, $\vec{n}_f$ and $\vec{n}_w$ point in different directions and the flux is discontinuous there. On the other hand, the velocity potential is continuous. The values of the

free surface velocity potential $\phi\left(P_f\right)$ and the value of the wall velocity potential flux $\phi_n\left(P_w\right)$ are given. Unknown velocity potential flux on the free surface $\phi_n\left(P_f\right)$ is obtained as a solution of the boundary element method.

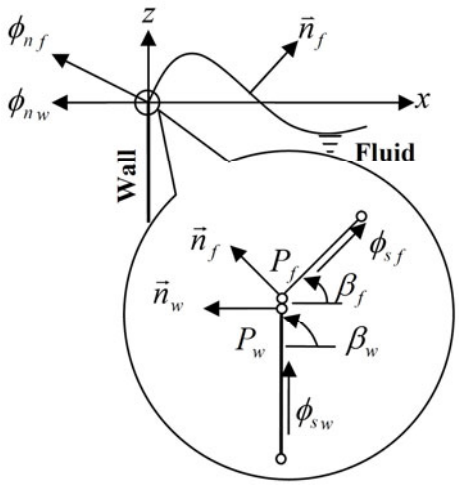

Fig. 2 Magnified view of intersection and the double node technique

The double node approach is applied to deal with the discontinuity of velocity potential flux at the intersection. The velocity of the fluid particle at the intersection $\vec{V}=\left(u,w\right)$ can be determined by the following equation:

$$\begin{bmatrix} u \\ w \end{bmatrix} = \begin{bmatrix} \cos\beta_w & -\sin\beta_w \\ \sin\beta_w & \cos\beta_w \end{bmatrix} \begin{bmatrix} \phi_{sw} \\ \phi_{nw} \end{bmatrix} = \begin{bmatrix} \cos\beta_f & -\sin\beta_f \\ \sin\beta_f & \cos\beta_f \end{bmatrix} \begin{bmatrix} \phi_{sf} \\ \phi_{nf} \end{bmatrix} \tag{23}$$

where ϕ_{sf} , ϕ_{sw} represent the tangential derivative of velocity potential on the free surface and the wall boundaries at the intersection point, respectively. The angles β_w and β_f correspond to the wall and the free surface angles with respect to the $+x$ direction determined by the following equation:

$$\tan\left(\beta_{w/f}\right) = \frac{\dfrac{\partial z}{\partial s_{w/f}}}{\dfrac{\partial x}{\partial s_{w/f}}} \tag{24}$$

where $\partial z/\partial s_{w,f}$ and $\partial x/\partial s_{w,f}$ are the tangential derivative of each point coordinate on the walls and the free surface boundaries, respectively. The tangential derivatives along the curvilinear free surface are approximated by the NURBS at each time step. The inflow boundary angle in front of the tank is $\beta_w=\pi/2$, while that of the wall boundary at the end of the wave tank is $\beta_w=3\pi/2$. The unknown derivative of the potential at the intersection point in Equation (23) can be obtained from the continuity of particle velocity as

$$\phi_{sf}=\phi_{nf}\frac{\cos\left(\beta_w-\beta_f\right)}{\sin\left(\beta_w-\beta_f\right)}-\phi_{nw}\frac{1}{\sin\left(\beta_w-\beta_f\right)} \tag{25}$$

2.7 Treatment of vortices on the trailing wake surface

If ϕ_t^+ and ϕ_t^- are the velocity potential at the upper and lower faces of the foil trailing edge, as shown in Figure 3, λ is the circulation around the foil and can be written as:

$$\lambda = \Delta\phi_t = \phi_t^+ - \phi_t^- \tag{26}$$

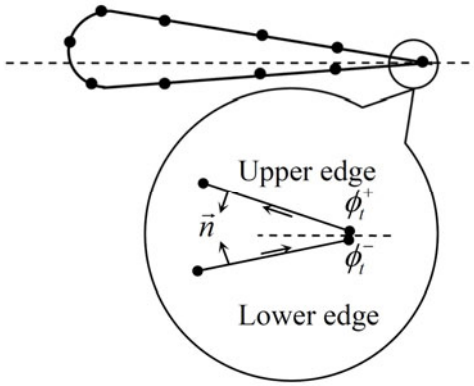

Fig. 3 Schematic diagram of the trailing edge treatment

The corner point problem on the trailing edge of the foil is addressed in the same way as that described for double points.

2.8 Discretization of boundary integral equation

Consider the linear elements on the inflow, outflow, and bottom boundaries and on the foil body ($\Gamma_1 \in S_i \cup S_w \cup S_b \cup S_h$) and the curvilinear elements on the free surface boundary ($\Gamma_2 \in S_f$). The boundary integral, Equation (9), is discretized as Equation (27). Γ_1 is divided into N_1 elements and Γ_2 is divided into N_2 high-order elements. Also, N_3 linear elements on the wake surface (S_t) are considered.

$$\begin{aligned} &c_i\phi_i + \sum_{j=1}^{N_1}\int_{\Gamma_j}\phi_j\frac{\partial G_{ij}}{\partial n}\mathrm{d}\Gamma_1 + \sum_{m=1}^{N_2}\int_{\Gamma_m}\phi_m\frac{\partial G_{im}}{\partial n}\mathrm{d}\Gamma_2 + \sum_{l=1}^{N_3}\int_{S_l}\Delta\phi_t\frac{\partial G_{il}}{\partial n^+}\mathrm{d}S \\ &= \sum_{j=1}^{N_1}\int_{\Gamma_j}\frac{\partial\phi_j}{\partial n}G_{ij}\mathrm{d}\Gamma_1 + \sum_{m=1}^{N_2}\int_{\Gamma_m}\frac{\partial\phi_m}{\partial n}G_{im}\mathrm{d}\Gamma_2 \end{aligned} \tag{27}$$

Curvilinear elements are denoted by m and linear elements by j and l. The boundary value at any point on the linear boundaries can be described by a linear interpolation function with respect to nodal values and coordinates of each element.

$$\Psi_{j/l}(\xi) = \begin{bmatrix} x_{j/l} \\ z_{j/l} \\ \phi_{j/l} \\ \phi_{n_{j/l}} \end{bmatrix} = \begin{bmatrix} x_1 & x_2 \\ z_1 & z_2 \\ \phi_1 & \phi_2 \\ \phi_{n_1} & \phi_{n_2} \end{bmatrix}_{j/l} \begin{Bmatrix} \lambda_1 \\ \lambda_2 \end{Bmatrix}, \quad \begin{matrix} j = 1,...,N_1 \\ l = 1,...,N_3 \end{matrix} \tag{28}$$

Ψ denotes the values of coordinates, velocity potential and potential flux on each element, respectively. ξ is the local coordinate varying from -1 to $+1$. λ_1, λ_2 are two linear interpolation functions:

$$\lambda_1 = \frac{1}{2}(1-\xi) \ , \ \lambda_2 = \frac{1}{2}(1+\xi) \tag{29}$$

For the element j, the integral on the left hand side of Equation (27) can be written as:

$$\int_{\Gamma_j} \phi_j \frac{\partial G_{ij}}{\partial n} \mathrm{d}\Gamma_1 = \int_{\Gamma_j} \left[\phi_1 \ \phi_2\right]_j \frac{\partial G_{ij}}{\partial n} \begin{Bmatrix} \lambda_1 \\ \lambda_2 \end{Bmatrix} \mathrm{d}\Gamma_1 = \left[\phi_1 \ \phi_2\right]_j \begin{Bmatrix} h_1^{ij} \\ h_2^{ij} \end{Bmatrix} \tag{30}$$

where $h_1^{ij} = \int_{\Gamma_j} \lambda_1 \, \partial G_{ij} / \partial n \, \mathrm{d}\Gamma_1$, $h_2^{ij} = \int_{\Gamma_j} \lambda_2 \, \partial G_{ij} / \partial n \, \mathrm{d}\Gamma_1$. Similarly, the integral on the right hand side of Equation (27) can be written as:

$$\int_{\Gamma_j} \frac{\partial \phi_j}{\partial n} G_{ij} \mathrm{d}\Gamma_1 = \int_{\Gamma_j} \left[\frac{\partial \phi_1}{\partial n} \ \frac{\partial \phi_2}{\partial n}\right]_j G_{ij} \begin{Bmatrix} \lambda_1 \\ \lambda_2 \end{Bmatrix} \mathrm{d}\Gamma_1 = \left[\frac{\partial \phi_1}{\partial n} \ \frac{\partial \phi_2}{\partial n}\right]_j \begin{Bmatrix} g_1^{ij} \\ g_2^{ij} \end{Bmatrix} \tag{31}$$

where, $g_1^{ij} = \int_{\Gamma_j} \lambda_1 G_{ij} \mathrm{d}\Gamma_1$, $g_2^{ij} = \int_{\Gamma_j} \lambda_2 G_{ij} \mathrm{d}\Gamma_1$.

The integral components $(h_1^{ij}, h_2^{ij}, g_1^{ij}, g_2^{ij})$ are evaluated by the Gaussian eight-point quadrature scheme. The free surface (S_f) can be approximated by the NURBS as a novel approach applied in the numerical wave tanks. The modelling and re-gridding of instantaneous free surface are carried out precisely due to the high-order curve. The velocity potential and its flux distribution on the free surface nodal point are described by the NURBS. For instance, each curve element is defined by taking four nodes for a third degree basis function. According to Equation (12), four curve rational functions $(\Re_1^{(3)}, \Re_2^{(3)}, \Re_3^{(3)}, \Re_4^{(3)})$ will be involved to discretize Green's boundary integrals.

$$\Psi_m(\xi) = \begin{bmatrix} x_1 & x_2 & x_3 & x_4 \\ z_1 & z_2 & z_2 & z_4 \\ \phi_1 & \phi_2 & \phi_3 & \phi_4 \\ \phi_{n_1} & \phi_{n_2} & \phi_{n_3} & \phi_{n_4} \end{bmatrix}_k \begin{Bmatrix} \Re_1^{(3)} \\ \Re_2^{(3)} \\ \Re_3^{(3)} \\ \Re_4^{(3)} \end{Bmatrix} \ , \ m = 1, ..., N_2 \tag{32}$$

Integral terms of the left hand side and the right hand side of Equation (27) for the free surface boundary part ($\Gamma_2 \in S_f$) can be carried out for the element m as:

$$\int_{\Gamma_m} \phi_m \frac{\partial G_{im}}{\partial n} \mathrm{d}\Gamma_2 = \int_{\Gamma_m} \left[\phi_1 \ \phi_2 \ \phi_3 \ \phi_4\right]_m \frac{\partial G_{im}}{\partial n} \begin{Bmatrix} \Re_1^{(3)} \\ \Re_2^{(3)} \\ \Re_3^{(3)} \\ \Re_4^{(3)} \end{Bmatrix} \mathrm{d}\Gamma_2 = \left[\phi_1 \ \phi_2 \ \phi_3 \ \phi_4\right]_m \begin{Bmatrix} h_1^{im} \\ h_2^{im} \\ h_3^{im} \\ h_4^{im} \end{Bmatrix} \tag{33}$$

$$\int_{\Gamma_m} \frac{\partial \phi_m}{\partial n} G_{im} \mathrm{d}\Gamma_2 = \int_{\Gamma_m} \left[\frac{\partial \phi_1}{\partial n} \ \frac{\partial \phi_2}{\partial n} \ \frac{\partial \phi_3}{\partial n} \ \frac{\partial \phi_4}{\partial n}\right]_m G_{im} \begin{Bmatrix} \Re_1^{(3)} \\ \Re_2^{(3)} \\ \Re_3^{(3)} \\ \Re_4^{(3)} \end{Bmatrix} \mathrm{d}\Gamma_2 = \left[\frac{\partial \phi_1}{\partial n} \ \frac{\partial \phi_2}{\partial n} \ \frac{\partial \phi_3}{\partial n} \ \frac{\partial \phi_4}{\partial n}\right]_k \begin{Bmatrix} g_1^{im} \\ g_2^{im} \\ g_3^{im} \\ g_4^{im} \end{Bmatrix} \tag{34}$$

The components ($h_1^{ik}, h_2^{ik}, h_3^{ik}, h_4^{ik}, g_1^{ik}, g_2^{ik}, g_3^{ik}, g_4^{ik}$) can be obtained in the same manner as those indicated in Equations (30) and (31). Boundary integral over the wake surface and the linear boundary are included in the influence matrix. Dipoles of constant strength are distributed on the linear element of the wake surface.

$$h_t^i = \sum_{l=1}^{N_3} \int_{S_l} \frac{\partial G_{il}}{\partial n^+} \mathrm{d}S \tag{35}$$

Then h_t^i is added to h_1^{ij}, corresponding to the upper edge element at the trailing edge, and subtracted from h_2^{ij} of the element on the lower trailing edge. The discretized form of Equation (27) for $\Gamma \in \left(S_i \cup S_w \cup S_b \cup S_f \cup S_h\right)$ can be written as:

$$c_i\phi_i + \left[\phi_1\ \phi_2\ \ldots\ \phi_N\right] \begin{Bmatrix} \hat{H}^{i1} \\ \hat{H}^{i2} \\ \vdots \\ \hat{H}^{iN} \end{Bmatrix} = \left[\frac{\partial \phi_1}{\partial n}\ \frac{\partial \phi_2}{\partial n}\ \ldots\ \frac{\partial \phi_N}{\partial n} \right] \begin{Bmatrix} F^{i1} \\ F^{i2} \\ \vdots \\ F^{iN} \end{Bmatrix} \tag{36}$$

where N is the total number of nodal points on the boundaries.

3. Numerical application

In this section, performance of the numerical wave tank is verified, first without a foil. The use of the NURBS in the free surface modelling and the updating of the NWT problem in the time domain make this study original. In the following, the performance of a foil beneath the wavy free surface is discussed. Computational results are validated with the analytical solution and compared with those of the past studies.

3.1 Numerical wave tank simulation

To investigate the influence of the free surface mesh size on the solution, a comparison between three different mesh sizes is drawn. A nonlinear second order Stokes wave of height ($2A = 5$ cm) and wave period ($T = 1$ s), is inputted at the inflow boundary to propagate downstream into the wave tank with a water depth of ($d = 0.5$ m) in the absence of a submerged body. In the damping zone 1, $\alpha = 1$ and $\beta = 1$ while in the damping zone 2, $\alpha = 1$ and $\beta = 2$. The uniform mesh sizes of the free surface $\Delta x = L/22$, $L/26$, and $L/30$ are considered, where $L = 2\pi/k$ is the wavelength. Also, the order of the NURBS basis function is $p = 3$. In each time step, the re-gridding scheme based on the NURBS approximates the free surface boundary and interpolates the same number of collocation points for the next time step. Evaluation of particle velocity for the time marching scheme is carried out through a derivative of the continuous NURBS basis function. For all runs, the time step Δt is set to $T/30$. The inflow and the outflow boundary are discretized into linear elements with a $d/20$ mesh size. The bottom boundary is divided by linear elements with a $L/10$ mesh size. In this test, twenty wave periods are generated and a numerical wave probe is deployed at $x = 3L$. Figure 4 shows the wave profile at the numerical wave probe for different meshes. It is found that solutions converge but the accuracy of computations to reach to the steady state depends on the nodal density on the free surface.

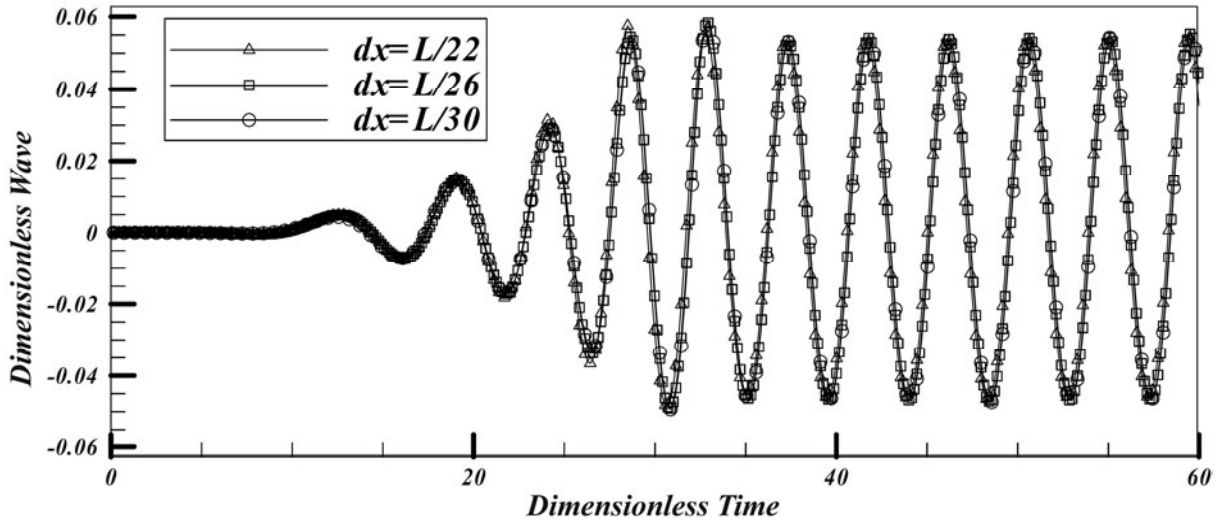

Fig. 4 Dimensionless free surface elevation (η/d) at x/L=3 due to a second order Stokes input wave of $k\eta$=0.104 versus dimensionless time $\left(t/\sqrt{(d/g)}\right)$, for $\Delta t=T/30$

The stability of the solution for a lengthy simulation is shown in Figure 5. For this purpose, the previous problem is solved with a smaller time step of $\Delta t = T/100$ and different free surface mesh sizes, $\Delta x = L/22$, $L/26$, and $L/30$, for twelve wave periods. It seems that the time step size is a significant factor for the convergence and accuracy of computations.

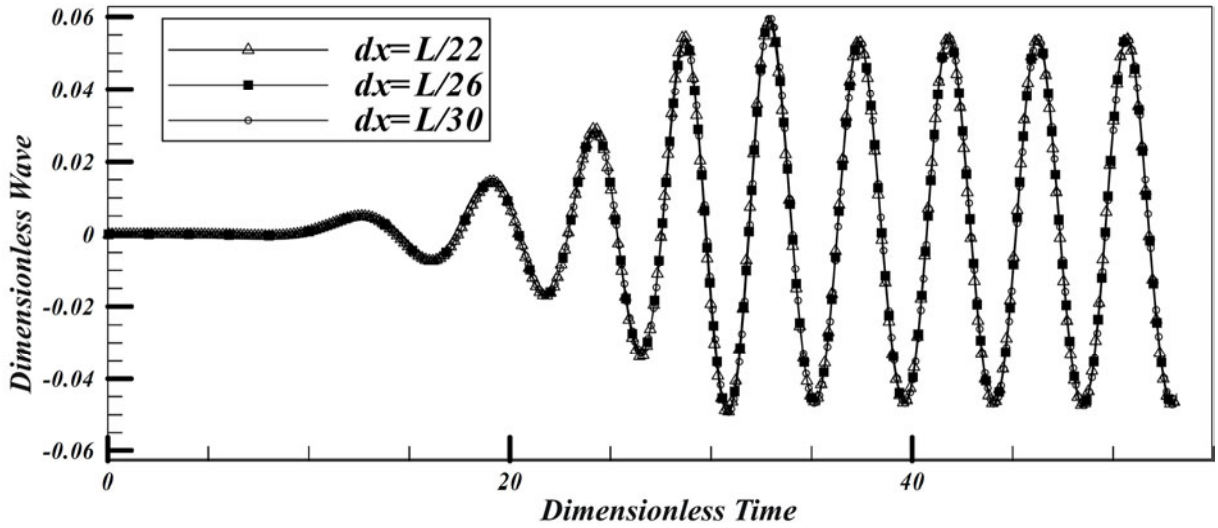

Fig. 5 Dimensionless free surface elevation (η/d) at x/L=3 due to a second order Stokes input short wave of $k\eta$=0.104 versus dimensionless time $\left(t/\sqrt{(d/g)}\right)$, for $\Delta t=T/100$

Simulation of previously discussed wave propagation problem is carried out for three time steps, $\Delta t = T/30$, $T/60$, and $T/90$, with a free surface mesh size of $\Delta x = L/22$. The wave elevation is simulated for 20 wave periods at $x = 3L$, as shown in Figure 6. It is found that solutions converge but the accuracy of the results for the steady state also depends on the time step size. To show the effect of the mesh size and time step size on the computation, the root mean square (RMS) error of the wave elevation is used.

$$RMS = \frac{1}{K}\sqrt{\sum_{i=1}^{K}\left\{\frac{\eta_i^{exact} - \eta_i^{num.}}{\eta_i^{exact}}\right\}^2} \tag{37}$$

where K is the number of time steps to complete one wave period at a fully developed wave condition in a fixed position and η denotes the analytical and numerical values of wave elevation.

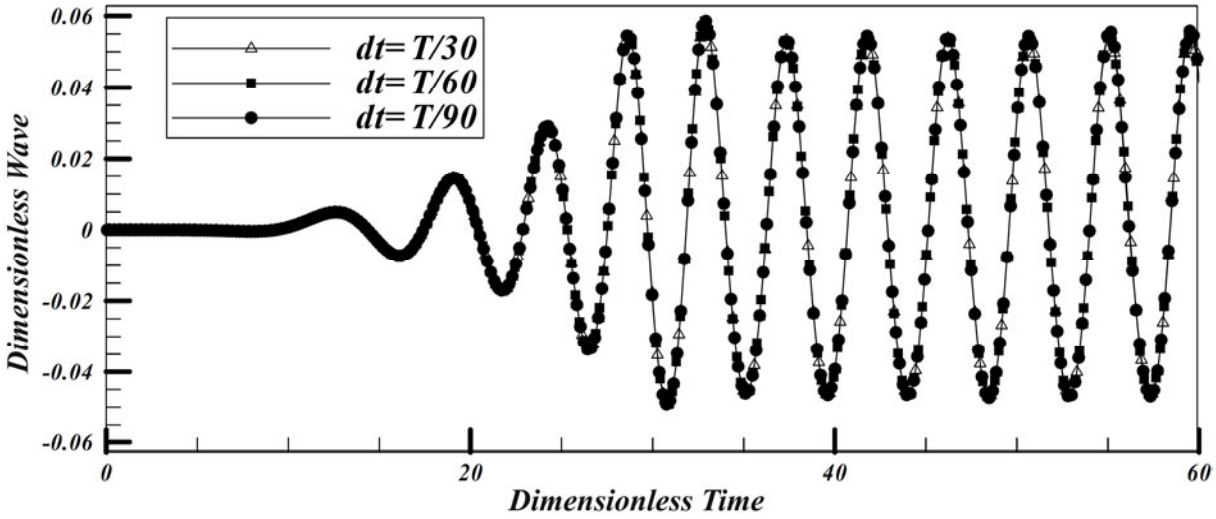

Fig. 6 Dimensionless free surface elevation (η/d) at x/L=3 due to a second order Stokes input short wave of $k\eta$=0.104 versus dimensionless time $\left(t/\sqrt{(d/g)}\right)$, for various time steps, calculated using a free surface mesh size of $\Delta x = L/22$

Figures 7 and 8 show the convergence of calculations for different mesh sizes and different time steps used in the previous simulation. It is shown that by increasing the mesh size by a fixed time step, the RMS increases. Also, for a fixed mesh size, the RMS increases by increasing the time step.

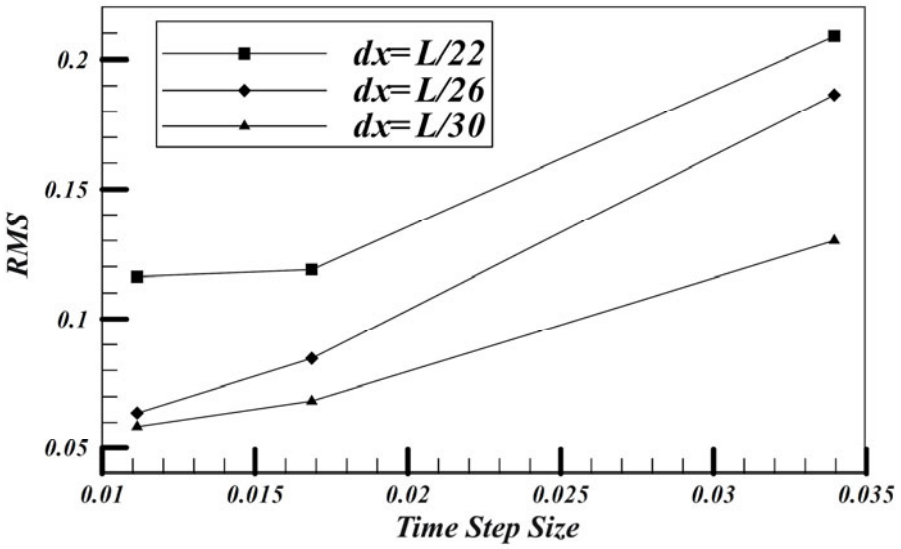

Fig. 7 RMS of wave elevation for different time step sizes and different mesh sizes, for a fully developed wave

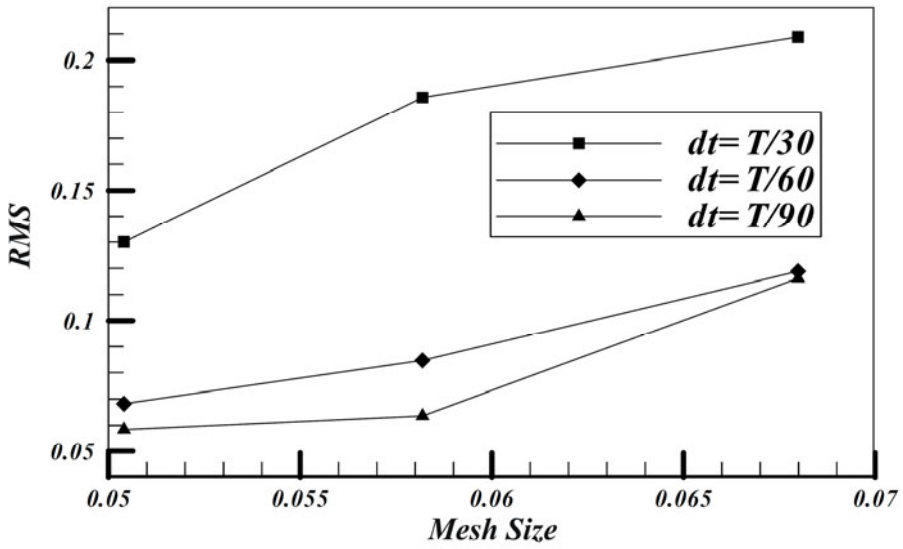

Fig. 8 RMS of wave elevation for different mesh sizes and different time steps, for a fully developed wave

Comparison between Figure 7 and Figure 8 shows that the RMS change becomes smaller for a smaller mesh size with $\Delta t = T/60$. A smaller time step size makes the numerical procedure time-consuming, while the solution error is not corrected substantially. Proper performance of NWTs mainly depends on damping zones. If the damping of wave energy is too weak, a certain amount of energy will come back to the computational domain from the downstream boundary. On the other hand, if the absorbing strength is too high, the damping zone will act as a solid boundary and waves will reflect from the outflow boundary. Figure 9 shows the free surface oscillations along the numerical tank from the inflow boundary (x/d)caused by the previous input of the second order Stokes wave. Mesh size of $\Delta x = L/30$ and a time step of $\Delta t = T/40$ are used in numerical modelling. In the damping zone 1, α and β are set to zero and in the damping zone 2, $\alpha = 1$ and $\beta = 2$.

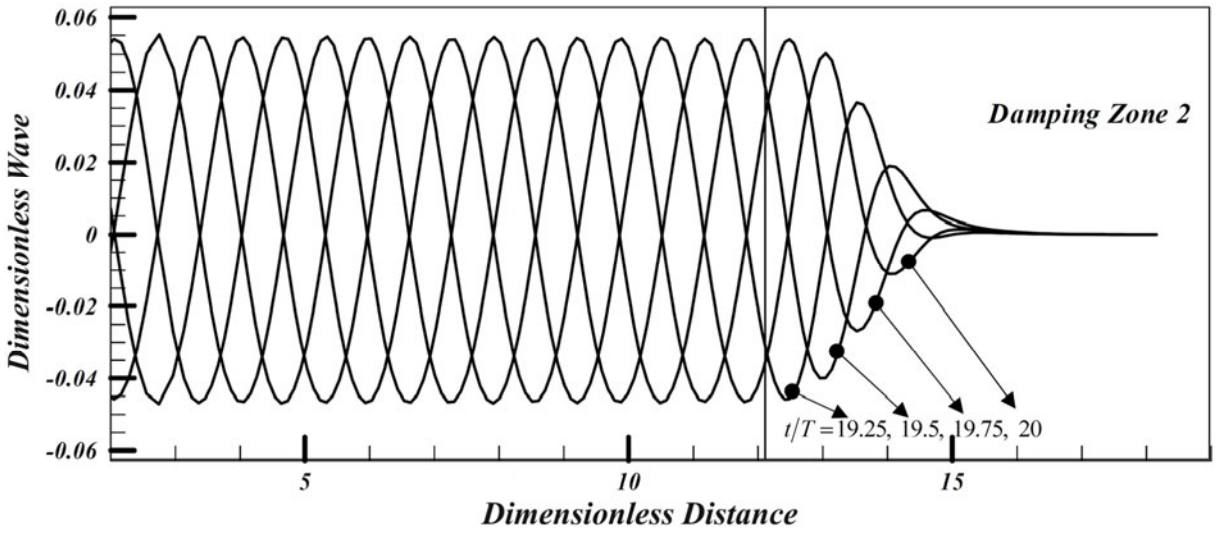

Fig. 9 The water surface elevation along the wave tank after the input of a second order Stokes short wave of $k\eta$=0.104, showing almost perfect damping (α=1, β=2)

This simulation is run for $t/T = 19.25$, 19.5, 19.75, and 20. It shows that the wave energy in the wave period is reduced until it is completely absorbed in the damping zone 2. When a wave crest in $t/T = 19.25$ enters the wave absorber, the wave height is damped gradually with time and finally the wave height vanishes. Also, a comparison is made between the

performance of the artificial beach parameter α (strength of absorption) and that of β (length of beach). Figure 10 shows a dimensionless wave elevation profile along the numerical wave tank for a fixed coefficient $\alpha = 1$ and different values of $\beta = 2,\ 3,\ 3.5$ for twenty wave periods. By choosing the mesh size and the time step size and the inflow absorbing zone to be similar to those in Figure 9, one can note in Figure 10 that the calm water region in the damping zone 2 is wider when β is increased.

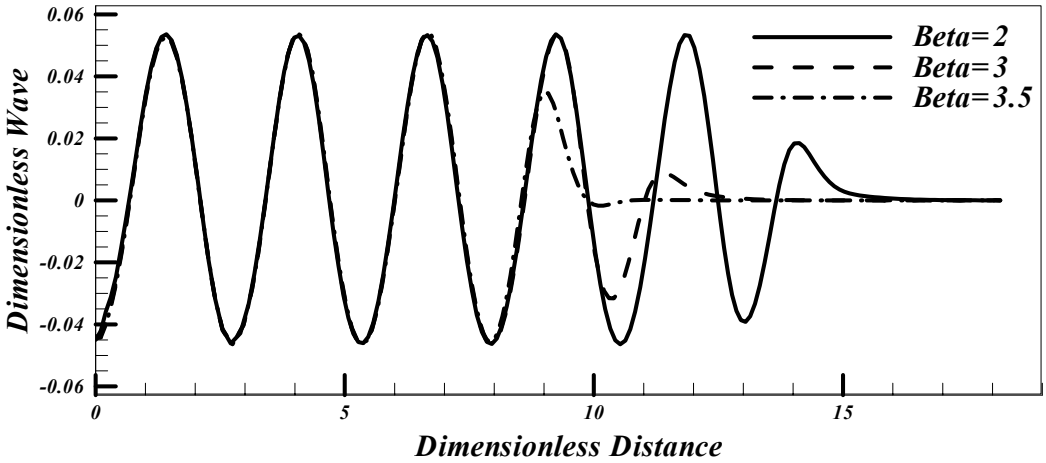

Fig. 10 Water surface elevations along the wave tank after the input of a second order Stokes short wave of $k\eta$=0.104 corresponding to different lengths of the damping zone 2 and α=1

Similarly, Figure 11 shows the wave elevation along the tank with $\alpha = 1,\ 0.5,\ 0.25$ and $\beta = 2$. It is shown that the input wave in the damping zone is vanishing rapidly when α is increased.

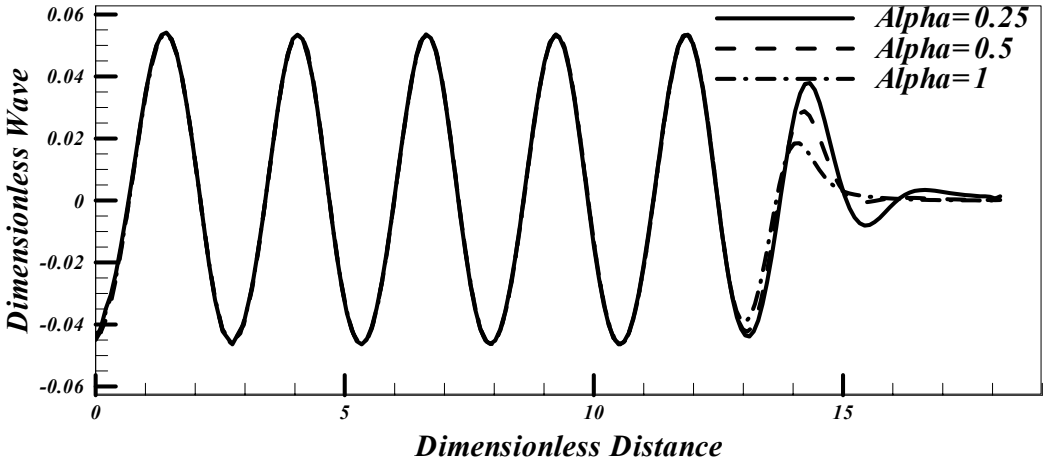

Fig. 11 Water surface elevations along the wave tank after the input of a second order Stokes short wave of $k\eta$=0.104 corresponding to different strengths of the damping zone 2 and β=1

Fluid volume, momentum and energy conservation test have been widely used to evaluate the precision of computations by a NWT. During the time domain simulation, the following values must be controlled:

$$M(t) - M(0) = \int_{\Gamma} \mathrm{d}v = \int_{S_f} \eta \mathrm{d}x \tag{38}$$

$$H(t) = \frac{\mathrm{d}M}{\mathrm{d}t} = \int_{S_i + S_f} \frac{\partial \phi}{\partial n} \mathrm{d}\Gamma \tag{39}$$

$$E(t)-E(0)=\rho\int_{\Gamma}\left(gz+\frac{1}{2}\nabla\phi\cdot\nabla\phi\right)\mathrm{d}v=\frac{1}{2}\rho\int_{S_i+S_f}\phi\frac{\partial\phi}{\partial n}\mathrm{d}\Gamma+\frac{1}{2}\rho g\int_{S_f}\eta^2\mathrm{d}x \qquad (40)$$

where M, H, E are the volume, momentum and energy of the fluid, respectively. The effects of the NURBS order p on the mean water level and on the change in the mass, momentum and total energy are shown in Figure 12. Mass conservation is the most significant parameter for testing the accuracy of the boundary integral equation and of the MEL approach. Therefore, an accurate definition of the boundary and an evaluation of the boundary value derivation are very important in the numerical procedure. Maximum errors have very small values. This shows that the NURBS can be applied accurately in the numerical wave tank simulation. It must be mentioned that variation in the change of above values is reduced when the order of NURBS increases and in the steady state, the volume conservation error should be zero. It seems that a NURBS NWT can be used to simulate wave flow problems appropriately.

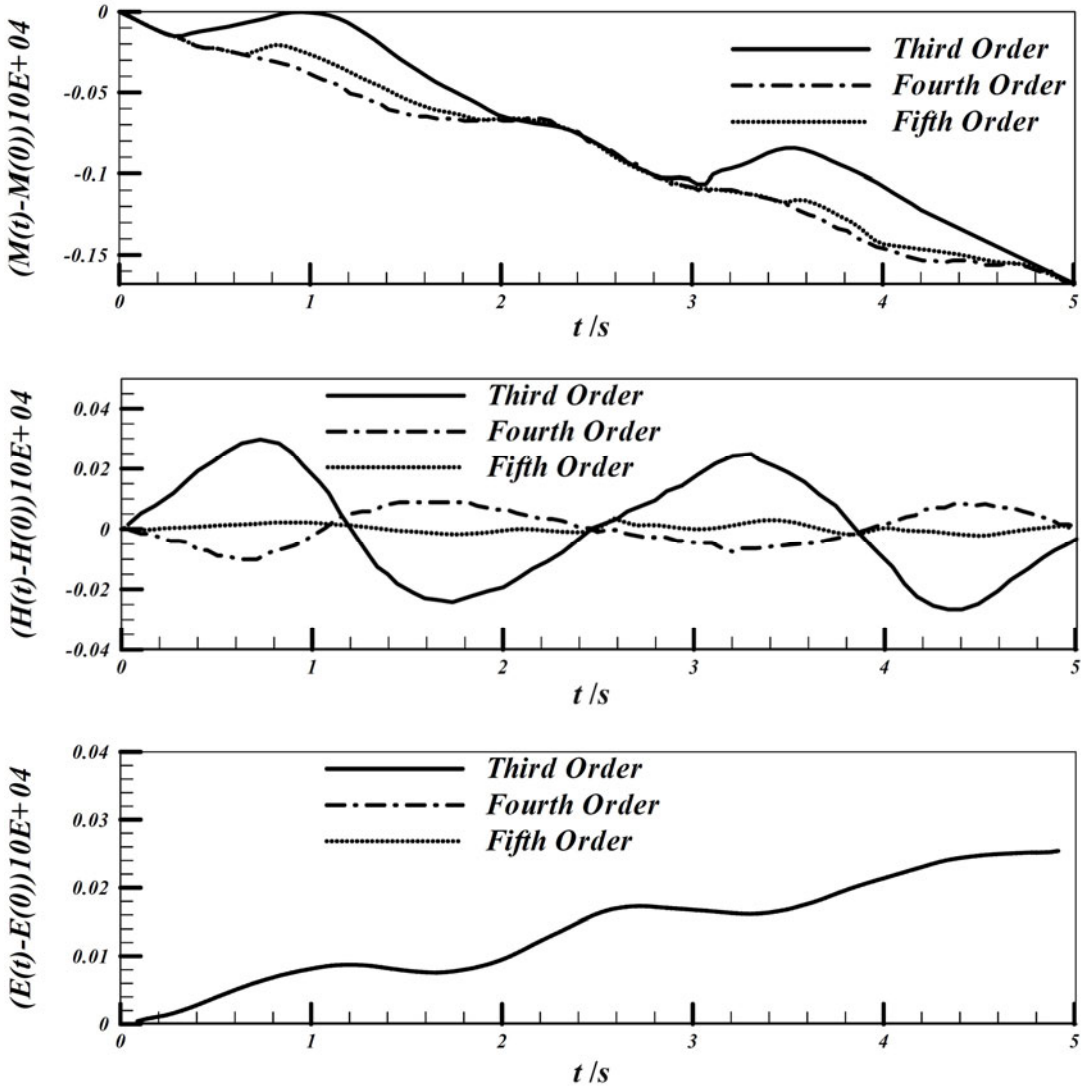

Fig. 12 Effect of the NURBS order on the change in the mass, momentum and energy conservation

Figure 13 compares the present numerical time history of water particle oscillation on the free surface at $x=3L$ with the analytical solution. The mesh size is $\Delta x=L/30$, time step size is

$\Delta t = T/60$ and the order of NURBS basis function is $p = 3$. It seems that the numerical solutions are in good agreement with the analytical results.

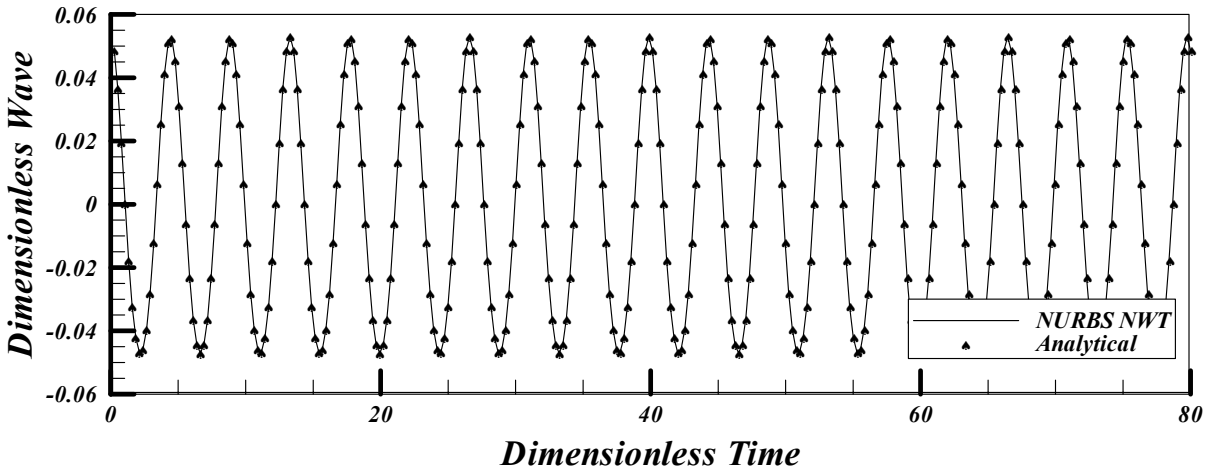

Fig. 13 Comparison between the time history of dimensionless water free surface elevation (η/d) obtained analytically and that of the present numerical solution at x=3L

3.2 Numerical results of hydrofoil problem

The hydrofoil used in this study is a NACA0015 with the chord length $c = 40$ cm, attack angle $\theta = 8^\circ$, and submergence depth $d_0 = 55$ cm. A wave with the amplitude $A = 4.8$ cm is generated from a wave maker at the end of the tank. The hydrofoil is exposed to the linear wave in the wave tank with the water depth $d = 71$ cm. In this condition, an unsteady force is exerted on the foil body. The Bernoulli equation gives pressure distribution over the hydrofoil body as

$$\frac{P}{\rho} = -\frac{\partial \phi}{\partial t} - \frac{1}{2}\nabla\phi \cdot \nabla\phi - gz \tag{41}$$

where the time derivation of potential velocity is approximated by the first order finite difference method over the hydrofoil body. By the surface integration of pressure in the directions x and z, the thrust (drag) and lift forces are obtained, respectively. The thrust and lift coefficients are defined as follows:

$$C_T = \frac{F_x}{\frac{1}{2}\rho\left(A\omega\right)^2 c} \tag{42}$$

$$C_L = \frac{F_z}{\frac{1}{2}\rho\left(A\omega\right)^2 c} \tag{43}$$

where F_x and F_z are the force components in the x and z directions, respectively. The mesh size and the time step are taken as $\Delta x = L/40$, $\Delta t = T/60$ and the third order NURBS basis function is adopted to model and re-mesh the free surface. The thrust coefficients computed from the present numerical wave tank are compared with the experimental results and the available linear and nonlinear numerical computations, as shown in Figure 14. It can be noted that for a high value of kc, the NURBS NWT solution differs significantly from experimental measurements but the difference grows smaller when the wave length increases. For the same

case as in Figure 14, the instantaneous lift and thrust coefficients are shown for $kc = 1.08$ in Figure 15. It is found that the maximum lift coefficient is achieved when the thrust (drag) coefficient has the minimum value.

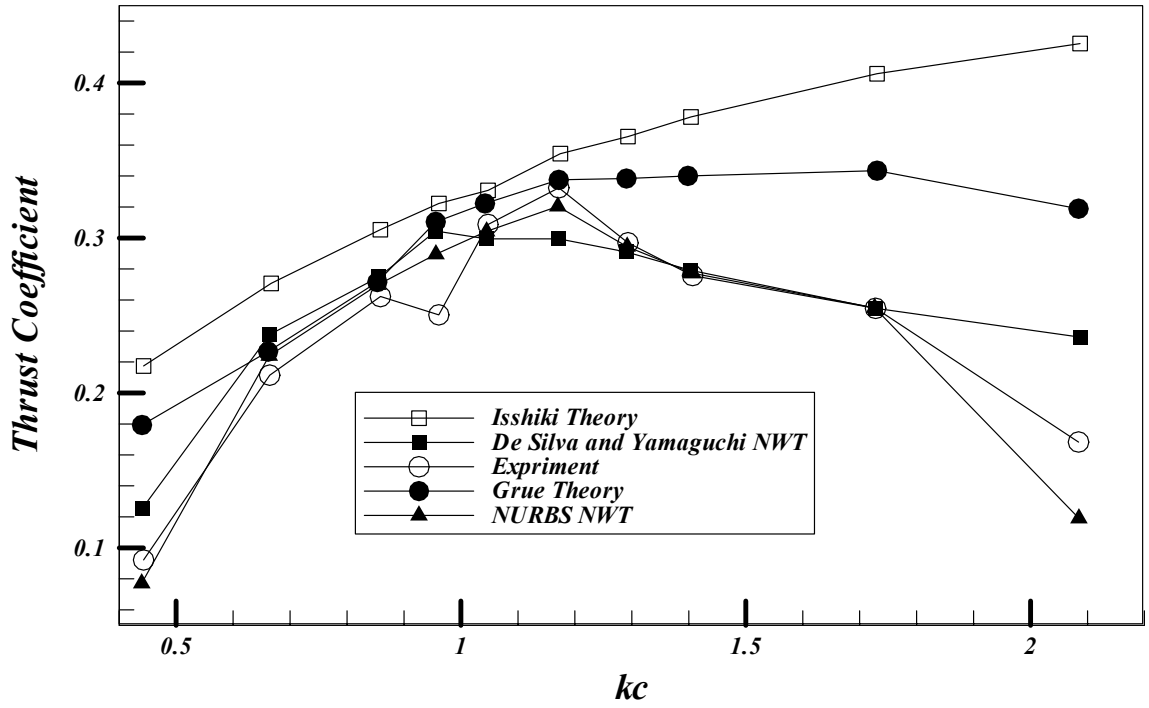

Fig. 14 Comparison of thrust coefficient between the experiment and the linear theory by Isshiki, the nonlinear theory by Grue et al. and De Silva and Yamaguchi NWT [5] and the present NWT versus different wave numbers

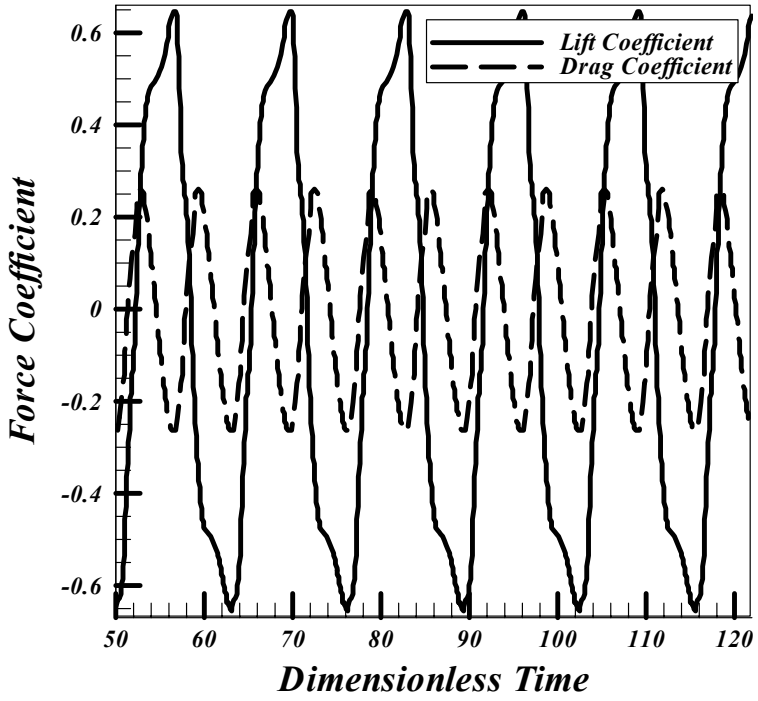

Fig. 15 Instantaneous lift and thrust coefficients for $kc = 1.08$

A snapshot of pressure distribution over the hydrofoil body at $t = 16.5$ s is presented in Figure 16. The positive pressure coefficient indicates the pressure side at the lower edge of

the hydrofoil and the negative one represents the suction side at the upper edge of the hydrofoil.

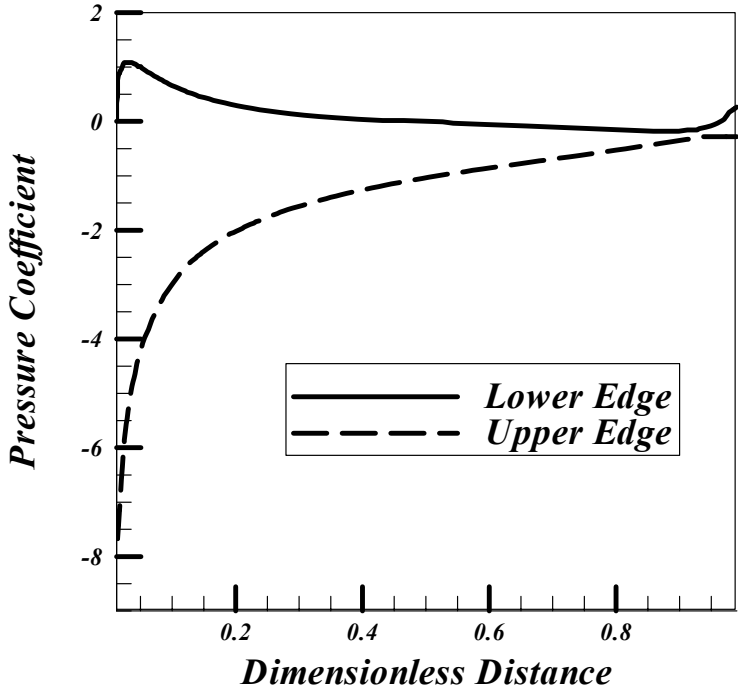

Fig. 16 Pressure coefficient $\left((p-p_{\infty})/(0.5\rho A^2\omega^2)\right)$ distribution over the foil body $\left((x-x_{L.E.})/c\right)$

4. Conclusion

Development of a high-order fully nonlinear two-dimensional NWT is considered in this paper. The simulation of a fully nonlinear wave using the NURBS formulation in a two-dimensional potential numerical wave tank is successfully completed. The MEL method and high-order boundary element method are employed in the numerical procedure. A high-order boundary integral equation based on Green's second identity is used to solve the Laplace equation in the Eulerian frame. NURBS formulation is employed to approximate the fluctuating free surface boundary and the regeneration of nodes. The material node approach and the fourth order Runge-Kutta time integration scheme compose the time marching scheme for the temporal updating of a fully nonlinear free surface boundary condition in the Lagrangian frame. The double-node technique is used to remove singularity at the corner nodes of computational domain to ensure the stability of the solution. To maintain the numerical accuracy and avoid instability in the MEL approach, the Chebyshev five-point smoothing scheme is applied every ten time steps. To obtain appropriate numerical solutions to the wave propagation problem in a numerical wave tank with a finite computational fluid domain, artificial damping zones (sponge layers) are deployed at the both ends of the tank. These damping zones are used to absorb progressively the wave energy in order to reduce the reflection from the ends of the wave tank into the computational domain. Perturbation sources are placed on the inflow boundary to generate the free surface oscillation during the simulation. Convergence and stability tests are performed for different mesh sizes and various time steps. The efficiency and performance of damping zones at the ends of the NWT were addressed. The changes in the mass, momentum and energy conservation are computed. The effects of the orders of the NURBS approximation on the results are presented and it is shown that the accurate solution can be obtained by the proposed procedure. Fluctuations in the computed values are reduced when the order of NURBS increases and in the steady state

condition, the volume conservation is satisfied. Volume and energy are less influenced by the order of basis function. The time history of a fully developed nonlinear Stokes wave in the NURBS NWT is compared with analytical results. The flow field about a hydrofoil located in the fully nonlinear wave tank was computed and horizontal and vertical force components are obtained. The present computational results are compared with the experimental and other numerical solutions and it is shown that the novel NWT procedure presented here gives accurate solutions. Also, the hydrofoil performance simulated in the time domain is shown by instantaneous forces and pressure distribution over the hydrofoil body.

REFERENCES

[1] S.F. Baudic, A.N. Williams, A. Kareem: *A Two-dimensional numerical wave flume-Part1; Nonlinear wave generation, propagation, and absorption*. OMAE Division and Presented at the 19th Int. Symp. And Exhibit on Offshore Mechanics and Arctic Engineering, New Orleans 2001.

[2] C.A. Brebbia, I. Dominguez: *Boundary elements: An introductory course*. WIT Press, UK 1992.

[3] B. Büchmann, J. Skouroup, K.F. Cheung: *Run-up on a structure due to second-order waves and a current in a numerical wave tank*. Appl. Ocean Res. 20, 297-308 (1998).

[4] R. Cointe: *Numerical simulation of a wave channel*. Eng. An. Bound. El. 7(4), 167-177 (1990).

[5] L.W.A. De Silva, H. Yamaguchi: *Numerical study on active wave devouring propulsion*. J. Mar. Sci. Technol. 17(3), 261-275 (2012).

[6] S.T. Grilli, I.A. Svendsen: *Corner problems and global accuracy in the boundary element solution of nonlinear wave flow*. Eng. Anal. Bound. El. 7(4), 178-195 (1990).

[7] K. Hamano, S. Murashige, K. Hayami: *Boundary elements simulation of large amplitude standing waves in vessels*. Eng. Anal. Bound. El. 27, 565-574 (2003).

[8] W. Koo: *Fully nonlinear wave-body interaction by a 2D potential numerical wave tank*. PhD Thesis, Texas A&M University, USA 2003.

[9] W. Koo, M.H. Kim: *Nonlinear wave-floating body interactions by a 2D fully nonlinear numerical wave tank*. Proceeding 14th International Offshore and Polar Engineering Conference, Toulon, France 2004: 23-28.

[10] M.S. Longuet-Higgins, E.D. Cokelet: *The deformation of steep surface waves on water (I)- A numerical method of computation*. Proceeding of The Royal Society of London 1976: 1-26.

[11] J.N. Newman: *Analysis of wave generators and absorbers in basins*. Appl. Ocean Res. 32(1), 72-81 (2010).

[12] L. Piegl, W. Tiller: *The NURBS Book*. 2nd ed. Springer, Germany 1990.

[13] S. Ryu, M.H. Kim, P.J. Lynett: *Fully nonlinear wave-current interactions and kinematics by a BEM-based numerical wave tank*. J. Comput. Mech. 32, 336-346 (2003).

[14] K. Tanizawa: *The state of the art on numerical wave tank*. Proceeding of 4th Osaka Colloquium on Seakeeping Performance of Ships, Japan 2000: 95-114.

[15] K.J. Tang, C.C. Huang: *Bragg reflection in a fully nonlinear numerical wave tank based on boundary integral equation method*. Ocean Eng. 35, 1800-1810 (2008).

[16] N.J. Wu, T.K. Tsay, D.L. Young: *Meshless numerical simulation for fully nonlinear water waves*. Int. J. Numer. Method. Fluid. 50, 219-234 (2005).

[17] L.F. Xiao, J.M. Yang, T. Peng, J. Li: *A meshless numerical wave tank for simulation of nonlinear irregular waves in shallow water*. Int. J. Numer. Method. Fluid. 61, 165-184 (2009).

[18] X.T. Zhang, B.C. Khoo, J. Lou: *Wave propagation in a fully nonlinear numerical wave tank: A desingularized method*. Ocean Eng. 33, 2310-2331 (2005).

Submitted: 11.8.2013

Accepted: 04.3.2015

Arash Abbasnia
Mahmoud Ghiasi
(Corresponding Author)
mghiasi@aut.ac.ir
Dept. Of Maritime Engineering
Amirkabir University of Technology
424 Hafez Ave.
15875-4413 Tehran Iran